



HAL
open science

Effects of high silicon contents on graphite morphology and room temperature mechanical properties of as-cast ferritic ductile cast irons. Part I – Microstructure

Rodolfo González-Martínez, Urko de La Torre, Jacques Lacaze, Jon Sertucha

► To cite this version:

Rodolfo González-Martínez, Urko de La Torre, Jacques Lacaze, Jon Sertucha. Effects of high silicon contents on graphite morphology and room temperature mechanical properties of as-cast ferritic ductile cast irons. Part I – Microstructure. *Materials Science and Engineering: A*, 2018, 712, pp.794-802. 10.1016/j.msea.2017.11.050 . hal-01982848

HAL Id: hal-01982848

<https://hal.science/hal-01982848>

Submitted on 16 Jan 2019

HAL is a multi-disciplinary open access archive for the deposit and dissemination of scientific research documents, whether they are published or not. The documents may come from teaching and research institutions in France or abroad, or from public or private research centers.

L'archive ouverte pluridisciplinaire **HAL**, est destinée au dépôt et à la diffusion de documents scientifiques de niveau recherche, publiés ou non, émanant des établissements d'enseignement et de recherche français ou étrangers, des laboratoires publics ou privés.




Open Archive Toulouse Archive Ouverte (OATAO)

OATAO is an open access repository that collects the work of Toulouse researchers and makes it freely available over the web where possible

This is an author's version published in: <http://oatao.univ-toulouse.fr/21399>

Official URL: <https://doi.org/10.1016/j.msea.2017.11.050>

To cite this version:

González-Martínez, Rodolfo and De la Torre, Urko and Lacaze, Jacques  and Sertucha, Jon *Effects of high silicon contents on graphite morphology and room temperature mechanical properties of as-cast ferritic ductile cast irons. Part I – Microstructure.* (2018) *Materials Science and Engineering A*, 712. 794-802. ISSN 0921-5093

Any correspondence concerning this service should be sent to the repository administrator: tech-oatao@listes-diff.inp-toulouse.fr

Effects of high silicon contents on graphite morphology and room temperature mechanical properties of as-cast ferritic ductile cast irons. Part I – Microstructure

Rodolfo González-Martínez^a, Urko de la Torre^a, Jacques Lacaze^b, Jon Sertucha^{a,*}

^a Investigación y Desarrollo de Procesos Metalúrgicos, IK4-Azterlan, Aliendalde Auzunea 6, E-48200 Durango, Bizkaia, Spain

^b CIRIMAT, Université de Toulouse, BP 44362, F-31030 Toulouse, France

ARTICLE INFO

Keywords:

High silicon ductile iron
Chunky graphite
Inoculation
Thermal analysis

ABSTRACT

Studying a series of near eutectic spheroidal graphite cast irons with various amounts of silicon up to 9.12 wt% confirmed that: 1. silicon stabilizes ferrite to such an extent that ferrite is the Fe-rich phase appearing during solidification at the highest silicon contents; 2. silicon triggers graphite degeneracy such as chunky graphite. As well-known, cerium and magnesium do also increase the risk of chunky graphite formation while antimony counteracts cerium. Based on the metallographic observations of the present work, an index is proposed to evaluate the risk of chunky graphite appearance from the silicon, magnesium, cerium and antimony contents. Above a critical value of this index, the risk for chunky graphite formation increases steadily. Using data from previous studies, it is further demonstrated that the critical value decreases with increase in casting modulus as expected. The evolution of mechanical properties of the prepared cast irons will be presented in a second part of this study.

1. Introduction

Among fully ferritic ductile irons, three new grades EN-GJS-450-18, EN-GJS-500-14 and EN-GJS-600-10 have been recently introduced in the European Standard EN-1563:2012. These cast iron grades have been defined as “solution strengthened ferritic ductile irons” as they are alloyed with silicon contents in the range 3.2–4.3 wt%. It has been reported that such high silicon contents promote high nodule count [1–3] and thus favor matrices with very high ferrite fractions. Such alloys have much higher strength than standard ferritic cast irons with comparatively low silicon contents though at the expense of lower ductility. On the other hand, the appearance of some graphite degeneracy such as chunky graphite has also been related to high silicon contents in ductile irons [4–7]. As for the mechanical properties, an optimum silicon content of 4.3 wt% has been reported on the basis of a limited number of alloys [8] which called for a more extensive study.

Accordingly, the present work reports results on 30 ductile cast irons with silicon contents ranging in between 2.29 and 6.14 wt% cast in standard Y2 keel-blocks (EN-1563). For helping to understand some of the features observed in high silicon cast irons, an additional alloy at 9.12 wt% silicon was also prepared and cast in similar conditions. The work is presented in two parts, this first one dealing with

metallographic investigation and characterization of the alloys, the second part to come with their mechanical properties at room temperature. Metallographic observations showed graphite degeneracy in some of the castings which appeared worth of a detailed presentation and discussion in comparison to literature information and previous results.

2. Experimental details

A series of 31 ductile cast iron alloys with varying silicon content were prepared in a medium frequency furnace (250 Hz, 100 kW) 100 kg in capacity. The metallic charges consisted of 20% low alloyed steel scrap and 80% low alloyed pig iron. Once melting process was completed, the composition was adjusted according to the required carbon and silicon contents by adding high purity graphite (> 99.0 wt% carbon) and a FeSi75 alloy (wt%, Si = 74.8, Ca = 0.30, Al = 0.76, C = 0.10 and Fe balance) respectively. A check of the melt composition was subsequently made and the melt temperature was then increased to 1510–1520 °C. Magnesium treatment was performed following the so-called sandwich method by transferring 50 kg of the prepared alloy to a ladle where FeSiMg alloy (grain size 5–25 mm, Si = 46.60, Mg = 6.00, Ca = 0.96, Al = 0.71 and rare earth RE = 0.92, Fe balance, wt%) had

* Corresponding author.

E-mail address: jsertucha@azterlan.es (J. Sertucha).

been positioned in an amount of 0.6 kg (1.2 wt% of the batch weight) and then covered with steel scrap (grain size 5–15 mm). After completion of the spheroidizing reaction, the alloys were skimmed and then cast in the moulds. An addition of 2.0–2.5 g Sb was made in the melting furnace to some of the batches (0.004–0.005 wt% of the batch weight) in order to study the effect of this element on graphite degeneracy in high silicon cast alloys.

The moulds were standard Y2 keel-blocks (EN-1563) which were manufactured with chemical bonded sand. Each mould contained one cavity in which 14 g (0.20 wt% of the total weight of the ductile iron alloy poured in the mould) of a commercial inoculant (grain size 0.2–0.5 mm, Si = 69.9, Al = 0.93, Ca = 1.38, Bi = 0.49, RE = 0.37 and Fe balance, wt%) was added before pouring the melt. Three particular castings were manufactured following a different inoculation procedure: casting #29 was not inoculated, casting #30 was inoculated with a smaller (0.15 wt%) and casting #31 with a higher (0.30 wt%) amount of the same inoculant.

After removing from the moulds, the keel-blocks were cleaned and test specimens were machined out from the bottom area to avoid the presence of shrinkage porosities and inclusions. Both a cylindrical specimen with 10 mm gauge diameter for tensile testing and several parallelepiped samples were obtained from this area. Pieces of these parallelepiped samples were used to perform DTA experiments, hardness measurements, X-ray diffraction (XRD) and scanning electron microscopy (SEM) characterizations.

After testing, one piece of the tensile specimens was used for chemical analysis of the alloys and to perform metallographic characterizations. Carbon and sulfur contents were measured by combustion analysis (LECO CS300) while the rest of analyzed elements were determined by the ICP-MS technique (Agilent 7500ce) after dissolving a metallic sample in a mixture of acids. The results obtained from these analyses are shown in Table 1 where two different carbon equivalent

Table 2
Criteria used for the classification of graphite particles.

Class	Circularity	Height-width Feret ratio
III	0.00–0.60	2.0–1000
V	0.50–0.77	1.0–1.5
VI	0.77–1.00	1.0–1.5

values were included according to Castro et al. [9] and the ASM handbook [10]. Most of the alloys are near eutectic, apart alloys #25 and #27 which are significantly hypoeutectic and alloy #28 which is strongly hypereutectic.

Metallographic analyses were performed close to the rupture surface of the tensile specimens. After polishing the samples, three representative pictures at 100× magnification (0.757 mm² each) per sample were taken without etching for image analysis of graphite using the ImageJ software. In this step, all graphite particles with an area equal to or higher than 15 μm² were counted, then assigned to class III, V or VI according to the ISO 945-1 standard and their area was measured. Classification of particles was carried out taking into account their circularity and their height-width Feret ratio [11] values using the criteria shown in Table 2. Those particles that could not be assigned to one of these classes by means of image analysis were then classified by visual analysis.

As it will be stated later, graphite particles classified in class III were considered as chunky graphite (CHG) except in case of the non-inoculated alloy #29 where degenerated graphite particles were identified as vermicular ones. The number and area of particles in each class were used for determining the number fractions (f_{CHG}^{count} , f_V^{count} and f_{VI}^{count}) and area fractions (f_{CHG}^A , f_V^A and f_{VI}^A). The final values reported later correspond to the average from the values measured in the three different fields. The nodule count was also determined from the number

Table 1
Chemical composition (wt%) of the cast alloys prepared in this work.

Alloy	C	Si	CE*	CE**	Mn	P	S	Cu	Cr	Ni	Ti	Sn	Mg	Ce	La	Sb
1	3.15	3.88	4.25	4.36	0.21	< 0.015	0.012	0.07	0.04	0.07	0.019	< 0.005	0.039	0.0059	0.0033	< 0.0005
2	3.16	4.11	4.32	4.44	0.20	< 0.015	0.011	0.05	0.04	0.06	0.020	< 0.005	0.039	0.0050	0.0026	< 0.0005
3	3.16	4.34	4.38	4.51	0.23	< 0.015	0.011	0.04	0.04	0.08	0.020	< 0.005	0.040	0.0064	0.0040	< 0.0005
4	3.10	4.45	4.36	4.49	0.21	< 0.015	0.012	0.05	0.04	0.05	0.020	< 0.005	0.040	0.0063	0.0034	< 0.0005
5	3.08	4.66	4.39	4.53	0.21	< 0.015	0.011	0.05	0.04	0.07	0.020	< 0.005	0.040	0.0061	0.0033	< 0.0005
6	3.13	3.94	4.24	4.36	0.29	0.020	0.010	0.03	0.04	0.06	0.077	< 0.005	0.036	0.0060	0.0035	0.0038
7	3.13	4.25	4.33	4.45	0.25	0.018	0.012	0.03	0.04	0.06	0.024	< 0.005	0.040	0.0060	0.0033	< 0.0005
8	3.10	4.45	4.36	4.49	0.25	0.019	0.013	0.03	0.04	0.07	0.020	< 0.005	0.039	0.0058	0.0031	0.0037
9	2.93	4.93	4.32	4.46	0.26	0.020	0.012	0.03	0.04	0.05	0.020	< 0.005	0.041	0.0061	0.0033	0.0028
10	2.93	5.11	4.37	4.52	0.26	0.019	0.013	0.03	0.04	0.05	0.022	< 0.005	0.036	0.0055	0.0030	0.0035
11	2.95	4.84	4.31	4.46	0.16	0.016	0.009	0.04	0.03	0.04	0.019	< 0.005	0.033	0.0055	0.0031	0.0040
12	2.91	5.04	4.33	4.48	0.18	< 0.015	0.010	0.04	0.04	0.06	0.019	< 0.005	0.035	0.0057	0.0031	0.0036
13	2.69	5.32	4.19	4.34	0.18	< 0.015	0.010	0.04	0.04	0.06	0.020	< 0.005	0.039	0.0059	0.0033	0.0040
14	2.72	5.55	4.28	4.45	0.20	< 0.015	0.010	0.04	0.04	0.06	0.020	< 0.005	0.033	0.0055	0.0031	0.0044
15	2.75	5.70	4.36	4.52	0.21	< 0.015	0.010	0.05	0.04	0.07	0.020	< 0.005	0.043	0.0062	0.0034	0.0039
16	2.71	5.15	4.17	4.32	0.19	0.019	0.009	0.07	0.03	0.09	0.018	< 0.005	0.043	0.0073	0.0044	0.0031
17	2.65	5.42	4.18	4.34	0.19	0.018	0.008	0.04	0.03	0.07	0.018	< 0.005	0.038	0.0078	0.0047	0.0031
18	2.75	5.36	4.26	4.42	0.20	0.017	0.010	0.04	0.03	0.05	0.019	< 0.005	0.040	0.0075	0.0042	0.0034
19	2.76	5.39	4.28	4.44	0.20	0.017	0.010	0.05	0.03	0.04	0.020	< 0.005	0.041	0.0079	0.0044	0.0029
20	2.77	5.56	4.34	4.50	0.20	0.018	0.010	0.04	0.04	0.06	0.018	< 0.005	0.034	0.0075	0.0045	0.0025
21	2.64	6.11	4.36	4.54	0.18	< 0.015	0.006	0.03	0.04	0.03	0.013	< 0.005	0.046	0.0063	0.0040	< 0.0005
22	2.71	6.14	4.44	4.62	0.18	< 0.015	0.006	0.03	0.04	0.03	0.012	< 0.005	0.044	0.0066	0.0042	0.0042
23	2.96	4.61	4.26	4.39	0.21	< 0.015	0.008	< 0.02	0.05	0.02	0.009	< 0.005	0.043	0.0045	0.0026	< 0.0005
24	2.90	4.60	4.19	4.33	0.22	< 0.015	0.007	< 0.02	0.06	0.02	0.009	< 0.005	0.036	0.0049	0.0029	0.0059
25	2.31	5.21	3.78	3.93	0.21	0.018	0.008	0.22	0.04	0.04	0.027	< 0.005	0.040	0.0068	0.0045	< 0.0005
26	3.67	2.29	4.32	4.39	0.18	0.018	0.006	0.04	0.04	0.03	0.025	< 0.005	0.035	0.0060	0.0039	< 0.0005
27	2.26	5.75	3.88	4.05	0.21	0.018	0.006	0.06	0.04	0.03	0.027	< 0.005	0.037	0.0060	0.0039	< 0.0005
28	2.41	9.12	4.97	5.24	0.21	0.018	0.008	0.04	0.04	0.03	0.027	< 0.005	0.032	0.0054	0.0040	< 0.0005
29	2.85	4.63	4.16	4.29	0.21	< 0.015	0.005	0.08	0.03	0.03	0.008	0.005	0.042	0.0048	0.0031	< 0.0005
30	2.93	4.74	4.27	4.40	0.19	< 0.015	0.005	0.07	0.02	0.03	0.008	< 0.005	0.045	0.0054	0.0034	< 0.0005
31	2.95	4.87	4.32	4.47	0.19	< 0.015	0.005	0.07	0.02	0.03	0.008	< 0.005	0.043	0.0053	0.0032	< 0.0005

CE* = C + 0.28Si + 0.007Mn + 0.092Cu + 0.303P [9].

CE** = C + 0.31Si - 0.027Mn + 0.076Cu + 0.33P + 0.40S [10].

count of particles in class V and VI, N_{V+VI} , or only in class VI, N_{VI} .

The metallographic samples were then etched using Nital 5% to check the amount of ferrite and pearlite. This also allowed detecting the presence of minor phases in some of the alloys. Some of the metallographic samples were deep-etched in order to partially remove the metallic matrix and to analyze the 3D graphite morphology. The deep-etching procedure consisted of an etching with a 40% HNO_3 aqueous solution for 60–90 s, followed by washing with a 50% HCl aqueous solution for a few seconds, both steps at room temperature. Scanning electron microscopy (SEM) was used to observe differences in graphite shape and distribution on the Nital-etched and the deep-etched samples. For this purpose, an Ultra Plus Carl Zeiss SMT apparatus with 0.8 nm resolution at 30 kV was employed. An X-Max 20 Oxford Instruments EDS detector with 120 eV resolution was used for determining the local chemistry.

Some alloys with various Si contents were subjected to Differential Thermal Analysis (DTA) using a SETARAM SETSYS 16/18 instrument. DTA specimens were cylinders 3.9 mm in diameter and 4–5 mm in length except for alloy #28 at 9.12 wt% Si when the sample was a small piece hammered out from one sample. Aluminium oxide powder was used to fill the reference holder. DTA runs consisted in heating to 1250 °C, holding at that temperature for 10 min and then cooling down to room temperature. The scanning rate upon heating and cooling was 10 °C/min.

X-ray diffraction (XRD) analyses were used to characterize the constituent phases in the different cast iron alloys prepared in the present work. These characterizations were carried out on a Bruker D8 Advance powder diffractometer using $\text{Cu-K}\alpha$ radiation (40 kV, 30 mA) with a Bragg-Brentano geometry with fixed slits and a graphite monochromator. The scanning range was 5–70° in 2θ (step: 0.03°, time per step: 2 s). The samples were prepared to obtain flat polished surface for analysis. Phase identification was performed using the DIFFRAC plus Evaluation software together with the PDF2 data base of the International Centre for Diffraction Data (ICDD).

3. Results

As it has been mentioned in the introduction, some level of degenerate graphite could be observed in an important number of the studied alloys. As a matter of fact, 19 of the 31 cast irons prepared in the present work were found to present this defect at various levels. The micrographs in Fig. 1 show examples where graphite degeneracy occurred at different intensities: low, medium, high and very high.

At higher enlargement as seen in Figs. 2a and 2b, degenerate graphite clearly appears as alignments of small graphite particles suggesting they are interconnected. This was demonstrated by deep etching of the metallographic sections as illustrated in Figs. 2c and 2d. Further, the characteristic features of these graphite precipitates show this is chunky graphite.

According to the standard nomenclature (EN-ISO 945-1), it can be considered that graphite particles of classes V and VI are counted as nodules. All the remaining graphite particles appear in class III and are associated with degenerate graphite which was identified as chunky graphite in all alloys but alloy #29. In this latter alloy, degenerate graphite was seen to be vermicular with $f_{III}^{count} = 0.12$ and $f_{III}^A = 0.25$. In all other alloys, f_{III} will be denoted as f_{CHG} . In Table 3 are reported the nodule counts and the number and area fractions of graphite in the three classes. Note that, because of the procedure used here, the lowest nodule counts are found in alloys with the highest amount of degenerate graphite.

All alloys were fully ferritic but alloy #26 which presented 3–5 surface % of pearlite, probably due to the comparatively low silicon content (2.29 wt%). The presence of minor phases in the metallic matrix is also reported in Table 3 by using three different comparative levels. In an important number of alloys, very low level of these minor phases were detected which are reported here as P_{FeSiC} and P_{TiC} (see

later in the text).

As pointed out in the introduction, higher silicon contents increase the risk of chunky graphite formation. This was verified in the present study and is further discussed in the next section. One of the ways to limit this effect of silicon is to add a small amount of antimony if some cerium is also present. This was verified in the present study where alloys with similar silicon content but with and without Sb addition showed lower and higher amount of degenerate graphite, respectively. Fig. 3 is a plot of the amount of chunky graphite, f_{CHG}^A , versus Si content where alloys with (open squares) and without (solid circles) Sb addition have been differentiated. Four alloys without any Sb addition and which are somehow out of the series are located with crosses: alloy #25 is highly hypoeutectic, alloy #28 is the one with more than 9 wt% Si and alloys #30 to #31 have received different inoculation treatment than the others. It is clearly seen that Sb addition decreases the amount of chunky graphite in alloys prone to its formation.

Although addition of inoculant has been reported as promoting chunky graphite formation [6,12,13], this effect still remains controversial. Thus, alloys #29, #30 and #31 were prepared using different inoculation additions, namely no addition, 0.15 wt% and 0.30 wt %, so as to check the effect of inoculation on chunky graphite formation. As mentioned above, the non-inoculated alloy #29 contains coarse and irregular vermicular graphite particles and not chunky graphite as illustrated in Fig. 4a. The comparison of results in Table 3 for alloys #30 (Fig. 4b) and #31 (Fig. 4c) reveals that chunky graphite areas increase significantly as inoculation does. This strong tendency could be related to the fact that increased inoculation leads to the increase in silicon and rare earth contents as well as to a lower undercooling during eutectic transformation [6].

A particular interest has been focused on microstructural features of alloy #28 with 9.12 wt% silicon where graphite particles are surprisingly quite well-formed nodules in most areas (Fig. 5a) though irregular ones similar to so-called exploded graphite are detected together with nodules in other locations (Fig. 5b). In this alloy also, two different minor phases have been detected, namely small faceted particles (Fig. 6a) and narrow precipitates (Fig. 6b).

EDS microanalysis was performed on these minor phases and compared to the analysis of the surrounding matrix. Compact faceted particles are mainly composed by Ti and C though peaks of Mo are often found, suggesting titanium carbide. They will be designated TiC particles. Analysis of the narrow precipitates and the matrix surrounding them showed peaks of Fe, Si and C, with the C peak of the matrix much smaller than for precipitates. It could be inferred this is an iron-silicon carbide such as the $\text{Fe}_8\text{Si}_2\text{C}$ phase previously selected to describe the metastable Fe-Si-C phase diagram [14]. This phase will be denoted FeSiC in the following. XRD analysis did not allow recording lines other than those associated with the matrix which was found to be B2-ordered bcc in alloy #28 in agreement with its high silicon content [14].

It could be noted that FeSiC precipitates were always located at ferrite grain boundaries which are the solidification grain boundaries as the alloy solidified with precipitation of ferrite from liquid. Moreover, TiC particles were more numerous away from graphite particles, though very seldom at ferrite grain boundaries. Because of the small size of both types of precipitates, it is very difficult to infer if they formed during solidification or by solid-state precipitation. As a matter of fact, thermodynamic calculations performed using the TCFE8 database and the ThermoCalc software showed TiC would not form at equilibrium for the Ti level of the present alloys. Its appearance must then relate to microsegregation build-up during solidification. The formation of the FeSiC phase is discussed in the next section.

Systematic SEM observation was performed to look for the presence of TiC and FeSiC precipitates in all alloys. The results are shown as P_{TiC} and P_{FeSiC} in Table 3 where this presence is classified as no, low, medium or high. It is noticed that TiC particles could be seen in all alloys without a clear correlation between Ti content and number of particles. On the contrary, a clear trend was found for FeSiC phase

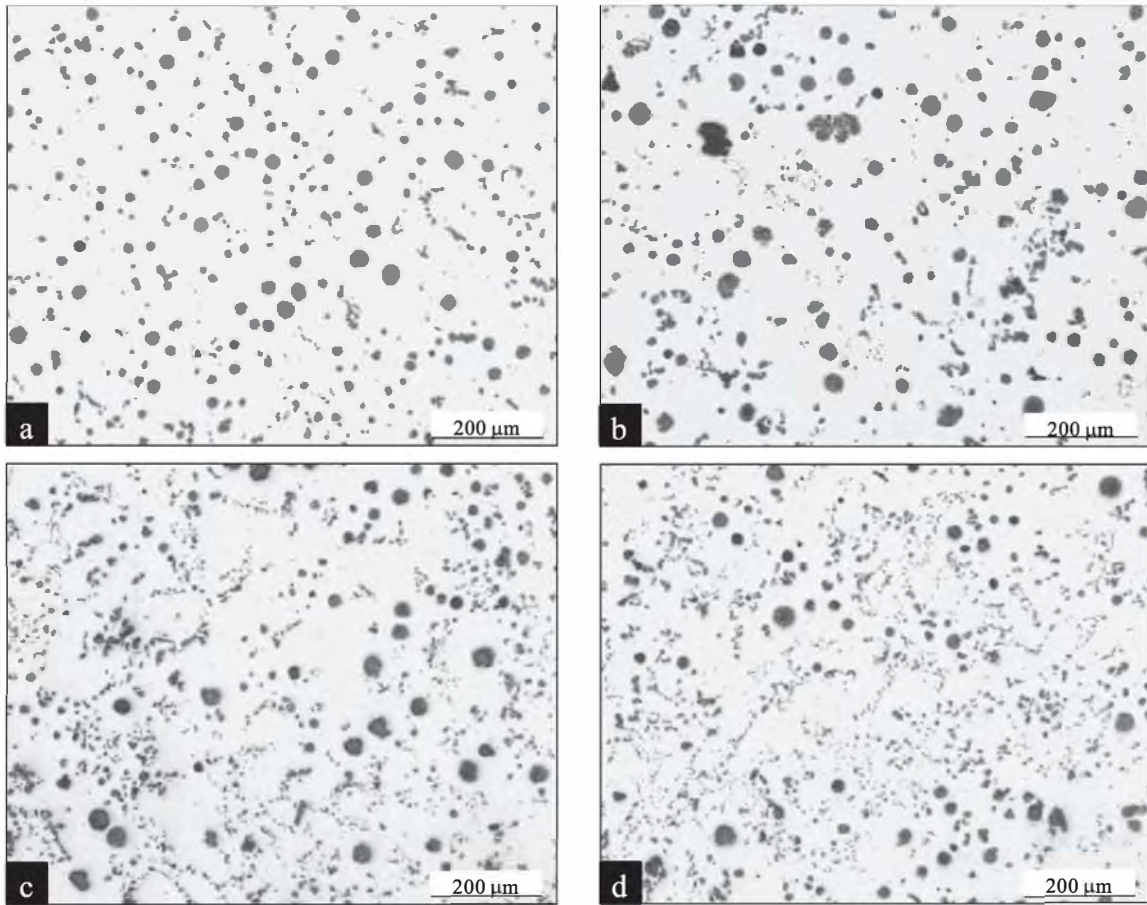


Fig. 1. Examples of degenerate graphite amount: (a) alloy #22 with $f_{CHG}^A = 0.11$, (b) alloy #1 with $f_{CHG}^A = 0.19$, (c) alloy #2 with $f_{CHG}^A = 0.34$ and (d) alloy #4 with $f_{CHG}^A = 0.39$.

which was generally observed at higher level with increased alloy silicon content. The maximum fraction of this phase was anyway quite low with a maximum at about 0.003–0.004 for alloy #28 (9.12 wt% Si).

Alloys #4 (4.45 wt% Si), #12 (5.04 wt% Si), #14 (5.55 wt% Si), #21 (6.11 wt% Si) and #28 (9.12 wt% Si) were subjected to DTA following the conditions indicated previously. Fig. 7 shows the set of DTA records in the upper temperature range when melting occurs. The main peak corresponds certainly to eutectic melting while the small peak that appears between 1145 °C and 1160 °C depending on the alloy probably relates to the reaction associated with melting of the iron-silicon carbide. In case of alloy #28, the sample was a broken piece and not a well machined cylinder. Accordingly, the DTA signal upon melting was smoother than for the other alloys but the same thermal arrest could definitely be observed when looking at the record with an enlarged scale.

DTA records for solidification showed features characteristic for solidification in the stable system, and in particular with no arrest that could relate to precipitation of FeSiC phase. Observation of the microstructure of these remelted alloys gave results much in line with a previous work [15] where the presence of chunky graphite in the original samples was correlated to the highest magnesium contents in the alloy. These results will be detailed and discussed elsewhere.

Fig. 8 presents the set of DTA records upon cooling in the temperature range of the eutectoid transformation. The temperature for the start of this transformation increases from about 850 °C to 970 °C when alloy's silicon content increases from 4 to 6 wt%, while no eutectoid transformation occurs in alloy #28 (9.12 wt% Si) because it is fully ferritic from solidification to room temperature. All records present a peak in between 600 °C and 725 °C corresponding to the magnetic Curie transition of ferrite, at a temperature that decreases with increasing

silicon content.

The eutectoid transformation has been characterized by the onset temperature and the values read in Fig. 8 are plotted in Fig. 9 with open circles. The peak temperature was used for the Curie transformation and the values are reported with closed circles in Fig. 9. For plotting these experimental values, the silicon content has been multiplied by 1.05 for accounting for graphite precipitation. These experimental values may be compared to calculations performed using ThermoCalc and the TCFE8 database for alloys containing 0.2 wt% Mn. The interrupted line is the calculated Curie temperature of ferrite which is seen to agree with experimental values. The solid line represents the lowest temperature of the austenite-ferrite-graphite three-phase field. This so-called T_{α} temperature is the one at which the eutectoid transformation is expected to start upon continuous cooling. It is seen that the eutectoid transformation starts with an undercooling of about 20 °C in quite a good agreement with previously reported data for a cooling rate of 10 °C/min. The dotted line represents the T_{α} temperature calculated as: $T_{\alpha} (^{\circ}\text{C}) = 739 + 18.4 \cdot w_{\text{Si}} + 2 (w_{\text{Si}})^2 - 45 \cdot w_{\text{Mn}}$ [16]. It is seen that this formula applies up to 4 wt% Si but would have to be corrected for higher values.

4. Discussion

The discussion of the above results will focus on two a priori different aspects, i) thermophysical properties of high-silicon cast irons and ii) the formation of degenerate graphite in the form of chunky graphite. Both of these aspects are however closely related to mechanical properties which will be dealt with in the second part of this work.

As a matter of fact, silicon is known to lead to ordering of the bcc structure of Fe-Si alloys (see appropriate references in the work by

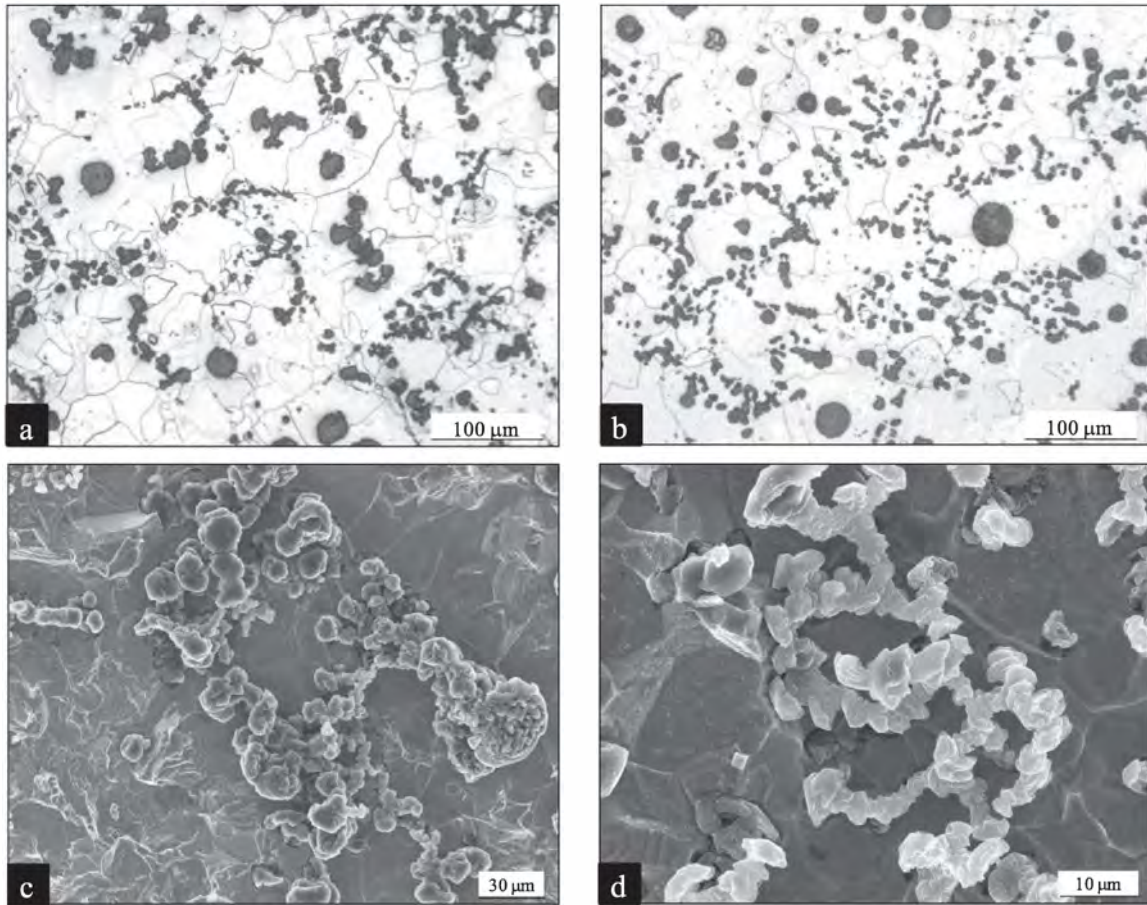


Fig. 2. High magnification optical micrograph of alloy #1 (a) and alloy #4 (b), and SEM micrograph of deep-etched alloy #2 (c) and alloy #5 (d).

Lacaze and Sundman [14]), and there is no doubt it has the same effect on ferrite in cast irons which contains very little carbon. As mentioned above, ordering could be detected by XRD analysis in alloy #28 at 9.12 wt% Si but it is guessed that partial ordering certainly takes place at lower silicon contents. When the alloy's silicon content is increased, ferrite is stabilized at higher and higher temperature and the eutectoid temperature is raised as illustrated in Fig. 9. According to the assessment of the Fe-C-Si system [14], alloys with nominal silicon content higher than 7 wt% should solidify with ferrite and graphite and not austenite and graphite. This is indeed what is observed with alloy #28 with a DTA thermal record that does not show any solid-state transformation (see Fig. 8).

Fig. 10 presents an Fe-C isopleth section of the stable Fe-Si-C system at 9 wt% Si. Under equilibrium, it is seen that solidification should totally proceed giving ferrite and graphite, but also that the $\text{Fe}_8\text{Si}_2\text{C}$ silicon-carbide which was considered in the assessment [14] appears at temperature below about 1050 °C. Though the validity of the thermodynamic assessment in this range of composition may be questioned as very little experimental information is available, Fig. 10 suggests that the narrow precipitates reported in this work could well have formed by solid-state precipitation.

Because chunky graphite has been reported to affect mechanical properties of cast irons, many attempts have been made to correlate its appearance with casting parameters known to favor or to hinder its formation. Casting modulus and inoculation have often been discussed, but the silicon content and the presence of low-level elements appear by far the most important issues. In many cases where the silicon content of the investigated alloys did not change much, the ratio of the amounts of cerium which promotes chunky graphite and of antimony that counteracts its effect has been considered [17,18]. Such a simple approach has been extended to account for other elements [19]. Also, a

statistical analysis of more than 60 castings having similar silicon contents but varying amount of Sb, Cu, Sn, Ce, La and P has been achieved with quite a good correlation coefficient [20], though not all of the predicted cross correlations between these low-level elements could be clarified.

Fig. 3 confirms that silicon promotes chunky graphite formation as already well established [4,5]. More specifically, this figure suggests that there is a risk for chunky graphite formation when the silicon content goes beyond some critical level, and it makes clear this level is increased when antimony is added. Antimony counteracts the effect of cerium by combining with it, while it does not tight magnesium which is also known to lead to similar graphite degeneracy than cerium when added in excess. Fig. 3 thus suggested looking for an index that would increase with silicon, cerium and magnesium content and decrease with antimony content. Further, it can be assumed that antimony is added at level such that it is totally tight by cerium. By trial and error, it was found that considering these two elements precipitate as CeSb_2 gives much better results than if this were CeSb . Finally, the following index could be proposed:

$$\Omega_{\text{Si}} = w_{\text{Si}} + 800 \cdot \left(w_{\text{Ce}} \cdot \frac{55}{140.1} - 2 \cdot w_{\text{Sb}} \cdot \frac{55}{121.8} \right) + 50 \cdot w_{\text{Mg}} \cdot \frac{55}{24.3} \quad (1)$$

where w_i is the content in wt% of element "i", and 55, 140.1, 121.8 and 24.3 are the atomic mass of cast iron, cerium, antimony and magnesium, respectively.

The Ω_{Si} index is plotted in Fig. 11 versus the f_{CHG}^A values given in Table 3, with solid circles for alloys without antimony added, open squares for alloys with antimony added and crosses for the same special castings as in Fig. 3. Apart for three of these special castings, it is seen that the results are fairly clustered with a steep increase in f_{CHG}^A when Ω_{Si} increases above a critical value of about 7.

Table 3

Microstructure data obtained from the cast irons prepared in the present work.

Alloy	N_{V_I} (mm^{-2})	N_{V+V_I} (mm^{-2})	f_{CHG}^{count}	f_V^{count}	$f_{V_I}^{count}$	f_{CHG}^A	f_V^A	$f_{V_I}^A$	P_{FeSiC}	P_{TiC}
1	302	462	0.13	0.29	0.58	0.19	0.30	0.50	—	Low
2	375	529	0.31	0.20	0.49	0.34	0.18	0.47	—	Low
3	372	548	0.33	0.21	0.46	0.31	0.23	0.45	—	Low
4	465	668	0.33	0.20	0.47	0.39	0.19	0.42	—	Medium
5	446	579	0.35	0.14	0.51	0.34	0.15	0.51	—	Medium
6	371	492	0.00	0.25	0.75	0.00	0.34	0.66	Low	Low
7	407	515	0.24	0.16	0.60	0.30	0.17	0.53	—	Low
8	538	644	0.02	0.16	0.82	0.04	0.19	0.77	Low	Low
9	448	538	0.15	0.14	0.70	0.18	0.13	0.69	Low	Low
10	493	614	0.01	0.19	0.79	0.02	0.19	0.79	—	Medium
11	388	474	0.00	0.19	0.81	0.01	0.22	0.77	—	Low
12	445	541	0.02	0.17	0.81	0.04	0.19	0.77	Low	Low
13	349	473	0.15	0.22	0.63	0.23	0.22	0.56	Medium	High
14	405	504	0.03	0.19	0.79	0.03	0.19	0.79	Medium	Low
15	463	613	0.11	0.22	0.67	0.15	0.21	0.65	low	Low
16	329	404	0.03	0.18	0.79	0.04	0.20	0.76	Medium	Low
17	253	325	0.14	0.19	0.67	0.21	0.17	0.62	Low	Medium
18	455	604	0.09	0.22	0.68	0.15	0.24	0.61	Low	Low
19	428	583	0.16	0.22	0.62	0.26	0.21	0.54	Low	Medium
20	389	498	0.25	0.16	0.59	0.33	0.17	0.50	Medium	Medium
21	119	143	0.87	0.02	0.11	0.65	0.06	0.29	Medium	High
22	377	457	0.08	0.16	0.76	0.11	0.15	0.74	Medium	Low
23	189	261	0.50	0.14	0.36	0.43	0.15	0.42	Medium	Medium
24	395	486	0.00	0.19	0.81	0.00	0.21	0.79	Medium	Low
25	113	179	0.02	0.36	0.61	0.06	0.43	0.51	Low	Medium
26	355	437	0.00	0.19	0.81	0.00	0.23	0.76	—	Low
27 (a)	41	54	0.96	0.01	0.03	0.88	0.03	0.09	Low	High
28 (b)	407	474	0.08	0.12	0.79	0.17	0.14	0.70	High	High
29 (c)	73	153	(c)	0.46	0.42	(c)	0.40	0.35	Low	Low
30 (d)	225	306	0.10	0.24	0.66	0.14	0.22	0.64	Medium	Low
31 (e)	220	270	0.62	0.07	0.31	0.57	0.08	0.35	Low	Low

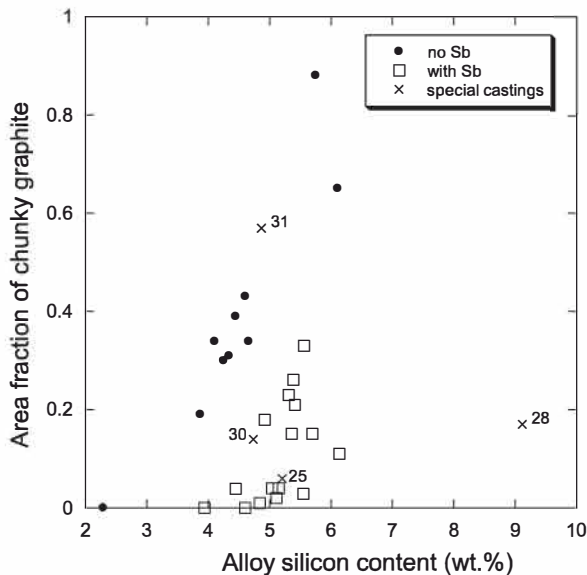
(a) Strongly hypoeutectic alloy.

(b) High silicon alloy.

(c) Non-inoculated alloy with vermicular graphite ($f_{III}^{count} = 0.12$ and $f_{III}^A = 0.25$).

(d) Inoculation at 0.15 wt%.

(e) Inoculation at 0.30 wt%.

**Fig. 3.** Amount of chunky graphite, f_{CHG}^A , versus silicon content. Numbers nearby the crosses are alloy number of four out-of-series castings (see text).

It may be stressed that accounting for the lanthanum content did not improve the result. Other elements that could affect graphite shape are sulfur, which was assumed to be totally tight by manganese, and phosphorus which did not vary enough in this work to allow for any effect to be evaluated.

The same approach was then applied to results obtained previously on heavy sections blocks (modulus 5 cm) cast without [21] and with cerium and antimony [18] additions. All alloys in these series of castings were near eutectic with a silicon content varying between 2.07 and 2.35 wt%. In these previous works, the extent of chunky graphite was evaluated with two parameters, V_V which indicated how much of the casting was affected by degenerate graphite, and A_A that was the area fraction of chunky graphite at the scale of the microstructure. This is this latter quantity that can be compared to f_{CHG}^A . The results of these previous studies are plotted with open symbols in Fig. 12 where they can be compared to the present results with solid symbols. The special castings of the present work have not been represented in this case. There is one point in the previous series that gives a very low index, it relates to a casting to which significant amount of antimony was added while very little cerium was present. As Fig. 11, Fig. 12 shows that the amount of chunky graphite increases when Ω_{Si} does. However, it is seen that the critical value is lower for these previous results, in between 4 and 4.5. This is assumed to be due to the larger modulus of the casting (defined as the ratio of the volume over the outer area of the casting) used in these previous studies as suggested with the arrow in Fig. 12.

A last comment concerns the fact that chunky graphite was not observed in the alloy at 9.12 wt% Si. It is guessed this is due to the fact that it solidifies with ferrite instead of austenite as Fe-rich phase. It would have been useful to discuss the possibility for coupled growth of chunky graphite and ferrite by considering the mechanical equilibrium between these phases and liquid at the solidification front, as already done for cast irons with lower level of silicon solidifying with austenite as Fe-rich phase [6]. However, the necessary interfacial energies between these three phases are not known for ferritic alloys with such a

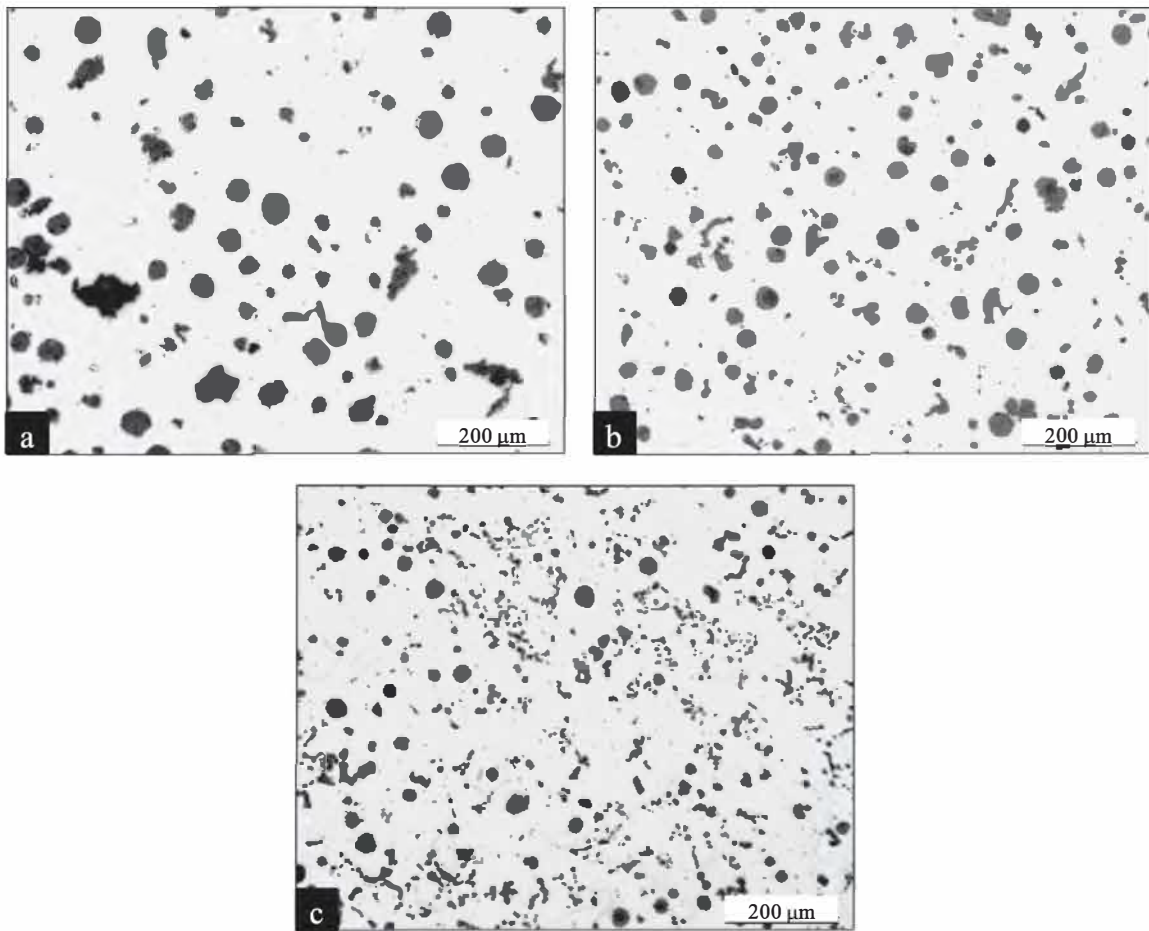


Fig. 4. Graphite morphology in alloy (a) #29 non-inoculated, (b) #30 inoculated with 0.15 wt% and (c) #31 inoculated with 0.30 wt%.

high silicon and carbon content.

5. Conclusion

Increasing silicon content of as-cast ferritic ductile irons has shown significant effects on the solidification of alloys and on resulting graphite morphology. A gradual stabilization of ferrite is obtained as silicon content is increased up to promoting the liquid to ferrite-graphite solidification in the alloy with the highest silicon content (9.12 wt%). Regarding graphite particles, important amounts of degenerated shapes assigned to chunky graphite have been obtained when increasing

silicon levels. In a number of alloys, antimony additions were effective for decreasing the formation of chunky graphite even at silicon contents higher than 6 wt%.

While not giving an explanation for chunky graphite formation, the present work proposes an index allowing for predicting the risk of such graphite degeneracy. The critical value of this index will be reached with increased amounts of silicon, cerium and magnesium, while addition of antimony decreases the risk. The most interesting aspect of the present approach is that it accounts for chemical combination of antimony and cerium which is expected to be the reason for the beneficial effect of the former. This opens up possibilities for extending to other

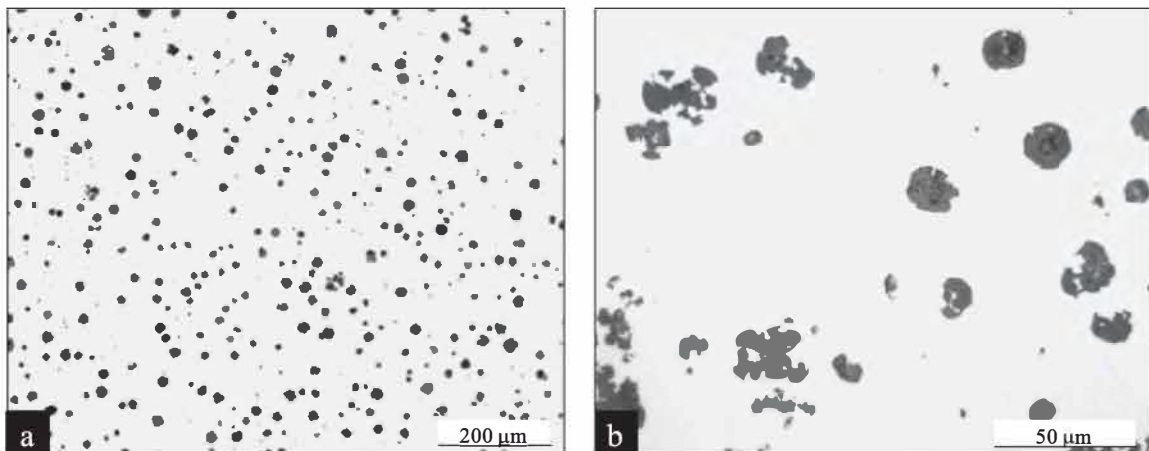


Fig. 5. (a) nodules distribution and (b) irregular graphite morphologies in alloy #28 (9.12 wt% silicon).

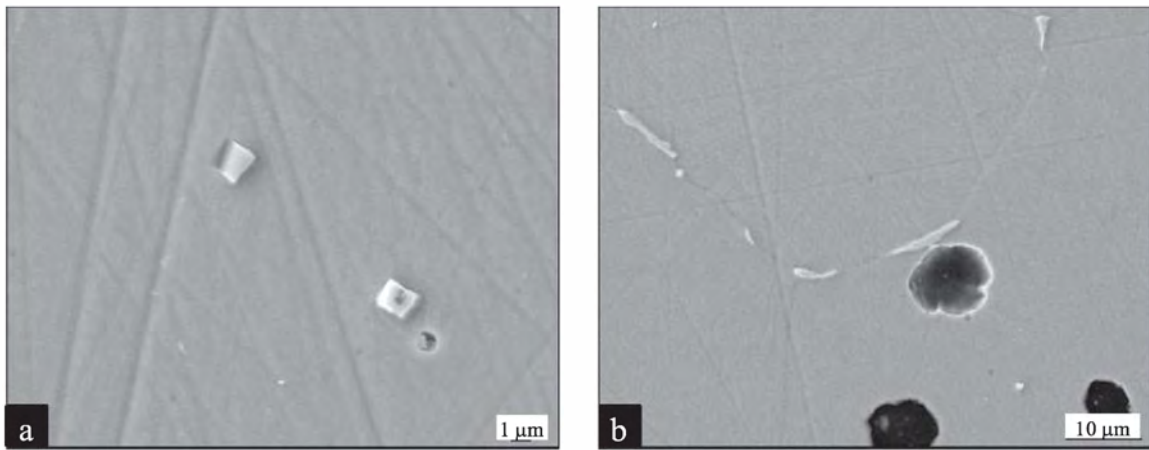


Fig. 6. (a) Faceted particles and (b) narrow precipitates at grain boundaries in alloy #28.

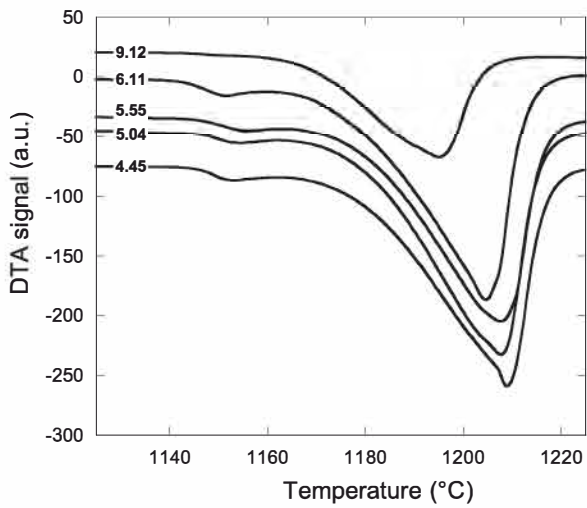


Fig. 7. DTA records in the range of temperature where melting occurs. Numbers refer to the alloy silicon content.

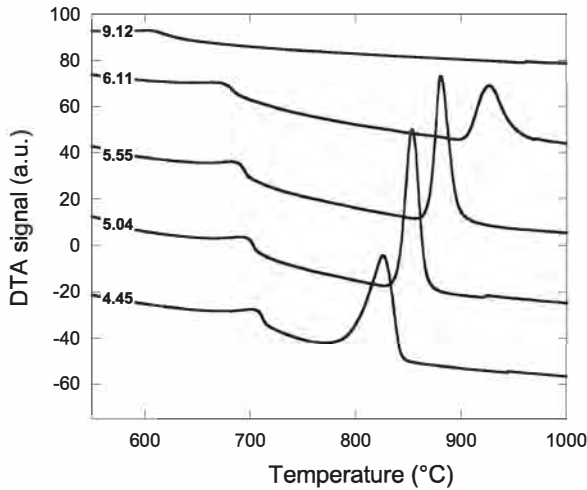


Fig. 8. DTA records upon cooling in the temperature range of the eutectoid transformation. Numbers refer to the alloy silicon content.

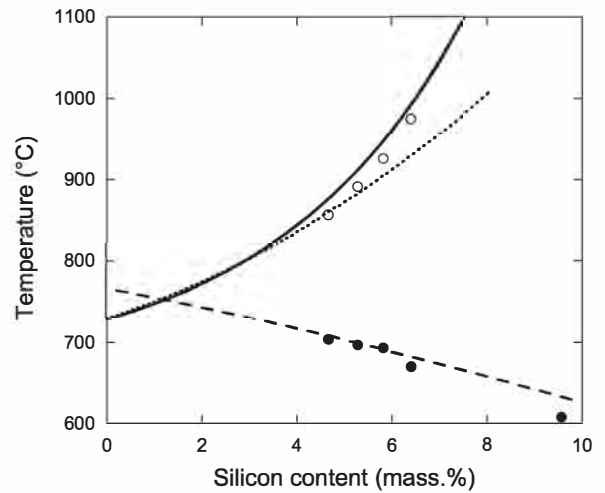


Fig. 9. Evolution with silicon content of the onset temperature for the eutectoid transformation upon cooling (open circles) and of the peak temperature of the Curie transition (solid circles). Lines are calculated, see text.

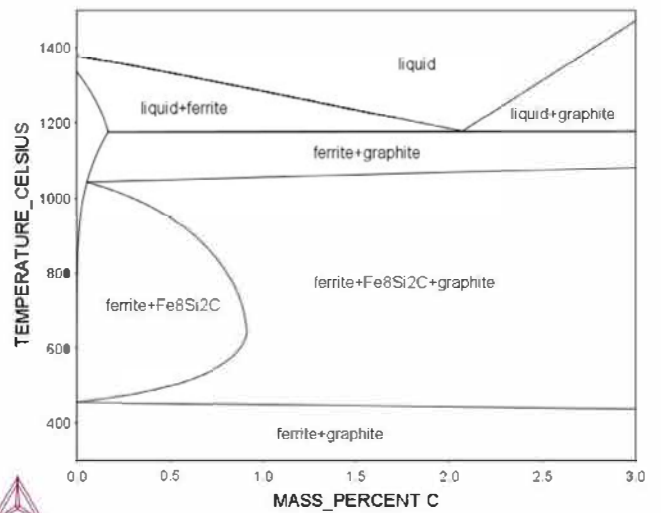


Fig. 10. Isoleth Fe-C section of the stable Fe-Si-C system at 9 wt% Si.

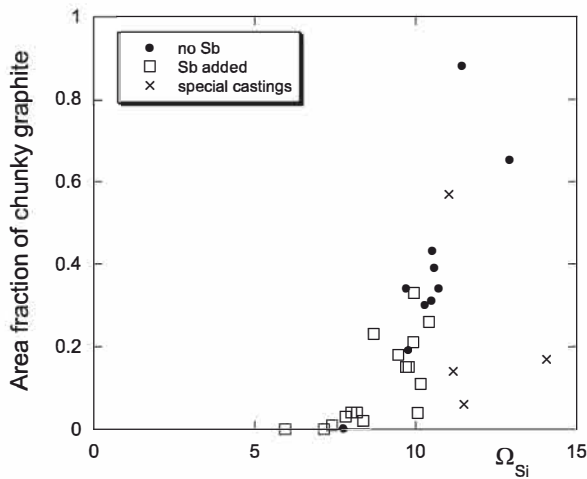


Fig. 11. Correlation between the index Ω_{Si} and the amount of chunky graphite f_{CHG}^A .

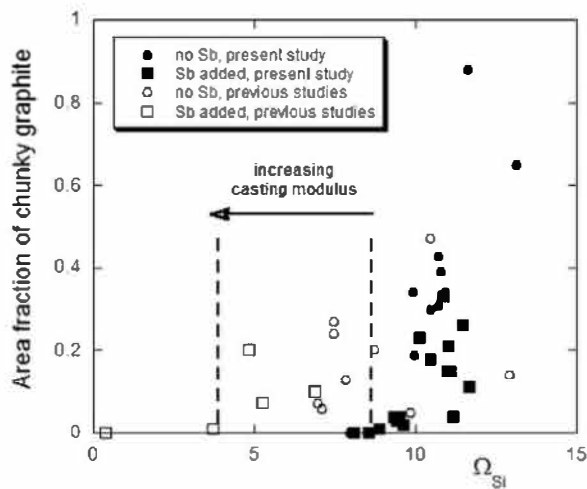


Fig. 12. Correlation between the index Ω_{Si} and the amount of chunky graphite as given by f_{CHG}^A for the present results and by A_A for previous results [18,21]. The vertical interrupted lines show that the critical index value decreases when the casting modulus increases.

low-level elements and could be sustained by the development of a corresponding thermodynamic database.

Acknowledgements

The authors want to thank TQC Technologies for experimental support. This research did not receive any specific grant from funding agencies in the public, commercial or not-for-profit sectors.

References

- [1] J. Khalil-Allafi, B. Amin-Ahmadi, Influence of mold preheating and silicon content on microstructure and casting properties of ductile iron in permanent mold, *J. Iron Steel Res.* 18 (2011) 34–39, [http://dx.doi.org/10.1016/S1006-706X\(11\)60034-4](http://dx.doi.org/10.1016/S1006-706X(11)60034-4).
- [2] P. Weiss, J. Brachmann, A. Bührig-Polaczek, S.F. Fischer, Influence of nickel and cobalt on microstructure of silicon strengthened ductile iron, *Mater. Sci. Technol.* 31 (2015) 1479–1485, <http://dx.doi.org/10.1179/1743284714Y.0000000735>.
- [3] U. de la Torre, A. Loizaga, J. Lacaze, J. Sertucha, As cast high silicon ductile irons with optimised mechanical properties and remarkable fatigue properties, *Mater. Sci. Technol.* 30 (2014) 1425–1431, <http://dx.doi.org/10.1179/1743284713Y.0000000483>.
- [4] J. Zhou, W. Schmitz, S. Engler, Untersuchung der gefügebildung von gusseisen mit kugelgraphit bei langsamer erstarrung, *Giessereiforschung* 39 (1987) 55–70.
- [5] B. Prinz, K.J. Eschborn, T. Schulze, R. Döpp, E. Schurmann, Untersuchung von ursachen von graphitentartungen bei gusseisen mit kugelgraphit in form von chunky-graphit, *Giessereiforschung* 43 (1991) 107–115.
- [6] U. de la Torre, J. Lacaze, J. Sertucha, Chunky graphite formation in ductile cast irons: effect of silicon, carbon and rare earths, *Int. J. Mater. Res. (formerly Z. Met.)* 107 (2016) 1041–1050, <http://dx.doi.org/10.3139/146.111434>.
- [7] J. Lacaze, L. Magnusson-Åberg, J. Sertucha, Review of microstructural features of chunky graphite in ductile cast irons, in: *Proceedings Keith Millis symposium*, Nashville, AFS, 2013, pp. 360–368.
- [8] W. Stets, H. Löblich, G. Gassner, P. Schumacher, Solution strengthened ferritic ductile cast iron properties, production and application, *Int. J. Metalcast.* 8 (2014) 35–40, <http://dx.doi.org/10.1007/BF03355580>.
- [9] M. Castro, M. Herrera, M.M. Cisneros, G. Lesoult, J. Lacaze, Simulation of thermal analysis applied to the description of the solidification of hypereutectic SG irons, *Int. J. Cast Met. Res.* 11 (1999) 369–374, <http://dx.doi.org/10.1080/13640461.1999.11819301>.
- [10] D. M. Stefanescu, J. Lacaze, Thermodynamics principles as applied to cast iron, in: *ASM Handbook*, vol 1A, Cast Iron Science and Technology, 2017, pp. 31–45.
- [11] L.R. Feret, *Assoc. Internat. Pour l'Essai des Mat.*, Zurich, 2 Group D, 1931.
- [12] Z. Ignaszak, Nodular graphite degeneration in the post-inoculated ductile iron, *Int. J. Cast Met. Res.* 16 (2003) 93–97, <http://dx.doi.org/10.1080/13640461.2003.11819565>.
- [13] I. Asenjo, P. Larrañaga, J. Sertucha, R. Suárez, J.M. Gómez, I. Ferrer, J. Lacaze, Effect of mould inoculation on formation of chunky graphite in heavy section spheroidal graphite cast iron parts, *Int. J. Cast Met. Res.* 20 (2007) 319–324, <http://dx.doi.org/10.1179/136404608X286138>.
- [14] J. Lacaze, B. Sundman, An assessment of the Fe-C-Si system, *Metall. Trans. A* 22 (1991) 2211–2223, <http://dx.doi.org/10.1007/BF02664987>.
- [15] J. Lacaze, I. Asenjo, S. Méndez, J. Sertucha, P. Larrañaga, R. Suárez, Experimental evidence for metallurgical modification associated to chunky graphite in heavy-section ductile iron castings, *Int. J. Metalcast.* (2012) 35–42, <http://dx.doi.org/10.1007/BF03355476>.
- [16] V. Gerval, J. Lacaze, Critical temperatures of spheroidal graphite cast irons: a review of literature data, *ISIJ Int.* 40 (2000) 386–392, <http://dx.doi.org/10.2355/isijinternational.52.2036>.
- [17] O. Tsumura, Y. Ichinomiya, H. Narita, T. Miyamoto, T. Takenouchi, Effects of rare earth elements and antimony on morphology of spheroidal graphite in heavy-walled ductile cast iron, *IMONO* 67 (1995) 540–545.
- [18] P. Larrañaga, I. Asenjo, J. Sertucha, R. Suarez, I. Ferrer, J. Lacaze, Effect of antimony and cerium on the formation of chunky graphite during solidification of heavy-section castings of near-eutectic spheroidal graphite irons, *Metall. Mater. Trans. A* 40A (2009) 654–661, <http://dx.doi.org/10.1007/s11661-008-9731-y>.
- [19] W. Stets, U. Petzschmann, R. Hentsch, A. Lötschert, Entstehung und Vermeidung von Chunkygraphit in Gusseisen mit Fugelgraphit, *Giesserei* 101 (2014) 36–47.
- [20] J. Sertucha, J. Lacaze, S. Armendariz, P. Larrañaga, Statistical analysis of the influence of some trace elements on chunky graphite formation in heavy section nodular iron castings, *Metall. Mater. Trans. A* 44A (2013) 1159–1162, <http://dx.doi.org/10.1007/s11661-012-1592-8>.
- [21] J. Sertucha, R. Suarez, I. Asenjo, P. Larrañaga, J. Lacaze, I. Ferrer, S. Armendariz, Thermal analysis of the formation of chunky graphite during solidification of heavy-section spheroidal graphite iron parts, *ISIJ Int.* 49 (2009) 220–228, <http://dx.doi.org/10.2355/isijinternational.49.220>.